

Application of discrete-element methods to approximate sea-ice dynamics

A. Damsgaard¹, A. Adcroft¹, and O. Sergienko¹

¹Program in Atmospheric and Oceanic Sciences, Princeton University, Princeton, New Jersey, USA

Key Points:

- Abrupt strengthening under dense ice-packing configurations induces granular jamming
- Cohesive bonds can provide similar behavior as Coulomb-frictional parameterizations
- A probabilistic model characterizes the likelihood of jamming over time

Abstract

Lagrangian models of sea-ice dynamics have several advantages over Eulerian continuum models. Spatial discretization on the ice-floe scale are natural for Lagrangian models and offer exact solutions for mechanical non-linearities with arbitrary sea-ice concentrations. This allows for improved model performance in ice-marginal zones. Furthermore, Lagrangian models can explicitly simulate jamming processes such as sea ice movement through narrow confinements. Granular jamming is a chaotic process that occurs when the right grains arrive at the right place at the right time, and the jamming likelihood over time can be described by a probabilistic model. While difficult to parameterize in continuum formulations, jamming emerges spontaneously in dense granular systems simulated in a Lagrangian framework. Here, we present a flexible discrete-element framework for approximating Lagrangian sea-ice mechanics at the ice-floe scale, forced by ocean and atmosphere velocity fields. Our goal is to evaluate the potential of simpler models than the traditional discrete-element methods for granular dynamics. We demonstrate that frictionless contact models based on compressive stiffness alone are unlikely to produce jamming, and describe two different approaches based on Coulomb-friction and cohesion which both result in increased bulk shear strength of the granular assemblage. The frictionless but cohesive contact model displays jamming behavior which is similar to the more complex model with Coulomb friction and ice-floe rotation at larger scales, and has significantly lower computational cost.

1 Introduction

Sea ice influences the atmosphere and ocean at high latitudes and thus the state of the climate throughout the globe [e.g. *Curry et al.*, 1995; *Deser et al.*, 2000; *Chiang and Bitz*, 2005]. In climate models, large-scale behavior of sea ice is typically simulated using (elastic-)viscous-plastic [e.g. *Thorndike et al.*, 1975; *Hibler*, 1979; *Hunke and Dukowicz*, 1997] or elastic-plastic continuum models [e.g. *Weiss et al.*, 2007; *Feltham*, 2008; *Girard et al.*, 2011; *Rampal et al.*, 2016]. Observations show that sea ice deformation in shear zones exhibits anisotropic properties [e.g. *Wilchinsky and Feltham*, 2006; *Girard et al.*, 2009; *Weiss and Schulson*, 2009]. However, in continuum models shear zones are greatly affected by grid resolution and mesh orientation [e.g. *Rudnicki and Rice*, 1975; *de Borst*, 1991]. The model behavior can be improved by using non-viscous rheologies and adaptive meshes [e.g. *Girard et al.*, 2011; *Rampal et al.*, 2016]. Moreover, continuum formulations

are generally not well-suited for simulating the ice-marginal zone, where spatial variability in sea-ice concentration and ice-floe thickness causes strong changes in mechanical properties. In such circumstances, continuum models do not simulate advection of a diverse ice pack correctly [e.g. *Horvat and Tziperman, 2015*].

1.1 Sea ice as a granular material

Previous studies argued that sea ice can be treated as a granular material, with a bulk rheology determined by the local mechanics and geometry of discrete and interacting ice floes [e.g. *Coon, 1974; Bak et al., 1988; Tremblay and Mysak, 1997; Hopkins, 2004; Feltham, 2005; Hopkins and Thorndike, 2006*]. In granular materials this behavior is called “self-organized complexity” as the overall behavior is governed by the local interactions and the resultant many-body response of the system [e.g. *Bak et al., 1988*]. Examples of granular phenomena include jets of sea-ice floes in the marginal-ice zone [e.g. *Feltham, 2005*], and jamming [*Samelson et al., 2006; Kwok et al., 2010; Herman, 2013; Rallabandi et al., 2017a,b*]. Mechanical rigidity of granular materials increases with the grain-packing density. Granular systems *jam* when this strengthening exceeds the driving stress, for example during flow through narrow conduits [e.g. *Cates et al., 1998; To et al., 2001; Zuriguel, 2014*]. In the cryosphere jamming is observed and modeled in icebergs in Greenlandic fjords [*Peters et al., 2015; Robel, 2017*], and controls the sea-ice flux through narrow confinements such as the Nares Strait between Greenland and Canada [e.g. *Kwok et al., 2010; Rallabandi et al., 2017a,b*]. Granular materials have a highly non-linear shear strength as a function of packing fraction or porosity. The non-linear granular rheology can cause jamming in continuum models [e.g. *Rallabandi et al., 2017a,b*], but does not capture the uncertainty associated with the jamming process. A probabilistic model can describe the likelihood of granular jamming [e.g. *Tang et al., 2009; Thomas and Durian, 2015*]. In the model proposed by *Tang et al. [2009]* the chance of survival P_s (the likelihood of the system to not undergo jamming) decreases exponentially with time t :

$$P_s = \exp(-t/T), \quad (1)$$

where the characteristic time scale of jamming T is dependent on the material, the experimental geometry and the forcing. The Mohr-Coulomb frictional coefficient μ_u that links shear stress τ_u with compressive normal stress N controls the mechanics of dense assemblages of granular materials:

$$\tau_u = C + \mu_u N, \quad (2)$$

73 where C is the material cohesion. This relationship is well established for granular mate-
 74 rials [e.g. *Terzaghi et al.*, 1996] and ice [*Schulson et al.*, 2006; *Fortt and Schulson*, 2007;
 75 *Weiss et al.*, 2007; *Feltham*, 2008; *Fortt and Schulson*, 2009; *Schulson and Fortt*, 2012].
 76 The effect of inertia on the post-failure rheology is described by the magnitude of the di-
 77 mensionless inertia number I :

$$I = \dot{\gamma} \bar{d} \sqrt{\frac{\rho}{N}}, \quad (3)$$

78 where $\dot{\gamma}$ is the shear-strain rate, \bar{d} is the representative grain diameter, and ρ is the grain
 79 density. For low values of the inertia number ($I \lesssim 10^{-3}$), granular rheology is essentially
 80 rate independent, and the Mohr-Coulomb frictional coefficient μ_u and dilative response is
 81 constant [e.g. *GDR-MiDi*, 2004]. For values of $I \gtrsim 10^{-3}$, granular materials behave as
 82 viscoplastic *Bingham materials*, with the frictional coefficient depending in a nonlinear
 83 fashion on the inertia number [*GDR-MiDi*, 2004; *da Cruz et al.*, 2005; *Jop et al.*, 2006;
 84 *Forterre and Pouliquen*, 2008], i.e. $\tau_u = \mu_u(I)N$. However, the $\mu_u(I)$ -rheology does not in-
 85 clude effects of non-locality [e.g. *Henann and Kamrin*, 2013], and, therefore, deformation
 86 is not distributed through material-dependent shear zones of finite width. Dilation repre-
 87 sents an additional complexity to granular shear zones with rigid particles, and is induced
 88 in dense packings as grains need space for relative movement [e.g. *Reynolds*, 1885; *Ned-*
 89 *derman*, 1992; *Terzaghi et al.*, 1996; *Tremblay and Mysak*, 1997; *Wilchinsky et al.*, 2010,
 90 2011]. The magnitude of dilation depends on material properties and the applied forcing
 91 [e.g. *Aharonov and Sparks*, 2002; *Damsgaard et al.*, 2013]. Continuum-modeling of dry
 92 and cohesionless granular materials is an area of active research and debate [e.g. *da Cruz*
 93 *et al.*, 2005; *Jop et al.*, 2006; *Forterre and Pouliquen*, 2008; *Henann and Kamrin*, 2013;
 94 *Bouzid et al.*, 2013]. For this reason we use particle-based Lagrangian methods for our
 95 sea-ice modeling, as individual ice-floe contact mechanics are more established than con-
 96 tinuum rheologies.

97 1.2 Numerical methods for granular materials

98 The discrete-element method (DEM, also known as the *distinct element method*) is
 99 widely used to model granular media and discontinuous materials in a variety of contexts
 100 [e.g. *Radjai and Dubois*, 2011]. The most popular approach is the *soft-body* DEM, origi-
 101 nally derived from molecular-dynamics modeling principles by *Cundall and Strack* [1979],
 102 where grain kinematics are determined by explicit temporal integration of their momentum
 103 balance. The DEM has been applied with discretizations on the sub-ice floe scale [*Hop-*

104 *kins et al.*, 1991], or with particles representing a collection of ice floes [*Li et al.*, 2014].
 105 Thus far, for sea-ice modeling the DEM is typically applied to simulate one ice floe per
 106 particle [e.g. *Gutfraind and Savage*, 1997a; *Hopkins*, 2004; *Herman*, 2016].

107 However, the DEM and other Lagrangian approaches to modeling sea-ice dynamics
 108 have not been used as components of global climate models, because of high computa-
 109 tional expense. Sea-ice models based on smoothed-particle hydrodynamics (SPH) have
 110 been proposed [e.g. *Gutfraind and Savage*, 1998; *Lindsay and Stern*, 2004], which offer
 111 better computational performance and Lagrangian discretizations. However, the complexity
 112 and kinematic phase transitions of granular materials are difficult to generalize in contin-
 113 uum formulations required for Eulerian models and SPH approaches [e.g. *Gutfraind and*
 114 *Savage*, 1997b; *Aharonov and Sparks*, 1999; *GDR-MiDi*, 2004; *da Cruz et al.*, 2005; *Mon-*
 115 *aghan*, 2012; *Bouzid et al.*, 2013].

116 The DEM is generally a computationally intensive approach. Due to the Lagrangian
 117 nature of the method, sophisticated neighbor-search algorithms are required to minimize
 118 the computational cost of contact mapping. Furthermore, the explicit temporal integration
 119 of the per-grain momentum balance is determined by the elastic wave speed through the
 120 granular assemblage, and thus requires short time steps for attaining numerical stability
 121 [e.g. *Krugger-Emden et al.*, 2008; *Radjai and Dubois*, 2011],

$$\Delta t \leq \frac{\epsilon}{\sqrt{\frac{\max(k_n)}{\min(m)}}}, \quad (4)$$

122 where ϵ is a safety factor (e.g. $\epsilon = 0.07$), $\max(k_n)$ is the largest elastic stiffness in the
 123 system, and $\min(m)$ is the smallest particle mass. As apparent from Eq. 4, small ice floes
 124 require small time steps, while softening of the elastic modulus can speed up the computa-
 125 tions. In order to increase the computational efficiency, it is common in DEM applications
 126 to both remove smaller grains and reduce the elastic stiffness of the grains, resulting in an
 127 increased time step length. The effect of these modifications can be assessed by evaluating
 128 the inertia number (Eq. 3). If it remains in the rate-independent regime of $I \lesssim 10^{-3}$, a
 129 grain-size increase and/or elastic softening will be inconsequential for the overall strength
 130 and dilative behavior of the granular system. If $I > 10^{-3}$ the shear stress and dilation will
 131 increase nonlinearly with increasing shear-strain rate [e.g. *GDR-MiDi*, 2004; *da Cruz et al.*,
 132 2005].

133 The goal of this study is to develop a numerical approach for simulating sea ice
 134 on the individual floe scale, which, at the same time, is computationally efficient enough
 135 to be used as a component of a climate model [e.g. *Griffies et al.*, 2005; *Delworth et al.*,
 136 2006; *Gnanadesikan et al.*, 2006]. To do so, we make methodological simplifications rel-
 137 ative to other discrete-element studies on sea ice, and explore the large-scale implications
 138 of different choices of contact rheology.

139 2 Methods

140 2.1 Governing equations

141 For computational efficiency, we treat the ice floes as cylinders moving in two di-
 142 mensions along the atmosphere-ocean interface. The ice-floe geometry is described by
 143 thickness h and horizontal radius r . The translational momentum balance for an ice floe
 144 with index i is:

$$m^i \frac{D^2 \mathbf{x}^i}{Dt^2} = \underbrace{\sum_j \left(\mathbf{f}_n^{ij} + \mathbf{f}_t^{ij} \right)}_{\text{Contact forces}} + \mathbf{f}_o^i + \mathbf{f}_a^i, \quad (5)$$

145 where m is the ice-floe mass, \mathbf{x} is ice-floe center position, and \mathbf{f}_n and \mathbf{f}_t is granular contact-
 146 normal and tangential force from interaction with ice floe j . The external forces \mathbf{f}_o and
 147 \mathbf{f}_a are ocean and atmosphere-induced drag, respectively. Similarly, the angular momentum
 148 balance for grain i is:

$$J_z^i \frac{D^2 \Omega^i}{Dt^2} = \underbrace{\sum_j \left(r^i \mathbf{n}^{ij} \times \mathbf{f}_t^{ij} \right)}_{\text{Contact torques}} + t_o^i + t_a^i. \quad (6)$$

149 J_z is the moment of inertia around the vertical center axis, and Ω is the angular position
 150 of ice floe i . The contact-normal unit vector is denoted \mathbf{n}_{ij} . The ocean and atmosphere
 151 can induce rotational torques t_o and t_a due to floe vorticity or ice-floe rotation. The forces
 152 and torques that appear in the linear and angular momentum balances are described below.
 153 In this study, and in the above equations for momentum, we disregard Coriolis forces, sea-
 154 surface slope, or wave action. These terms should be considered when implementing in
 155 coupled models, but are omitted here due to the idealized ocean and atmosphere in our
 156 simulation setups. We integrate the momentum-balance equations in time using a third-
 157 order Taylor expansion scheme, which is computationally simple and has a high level of
 158 numerical precision [e.g. *Krugger-Emden et al.*, 2008].

159 In this study, we compare the jamming behavior of two differing ice-floe contact
 160 models. Common to both models is f_n , the resistive force to axial compressive strain
 161 between two cylindrical ice floes i and j , which is modeled by (Hookean) linear elasticity
 162 based on the overlap distance δ_n :

$$f_n^{ij} = A^{ij} E^{ij} \delta_n^{ij} \quad \text{when} \quad 0 > |\delta_n^{ij}| \equiv |\mathbf{x}^i - \mathbf{x}^j| - (r^i + r^j). \quad (7)$$

163 This is a common approach in discrete-element simulations [e.g. *Cundall and Strack*, 1979;
 164 *Luding*, 2008; *Ergenzinger et al.*, 2011; *Damsgaard et al.*, 2016, 2017]. The contact cross-
 165 sectional area $A^{ij} = R^{ij} \min(h^i, h^j)$ is determined by the harmonic mean $R^{ij} = 2r^i r^j / (r^i +$
 166 $r^j)$ of the ice-floe radii r^i and r^j , as well as the smallest of the involved ice-floe thick-
 167 nesses h^i and h^j . The harmonic mean of Young's modulus E^{ij} scales the linear-elastic
 168 force resulting from axial strain of a distance $|\delta_n^{ij}|$. The stiffness is scale invariant [e.g.
 169 *Obermayr et al.*, 2013], and assumes constant elastic properties of the ice itself, regard-
 170 less of ice-floe size. We note that nonlinear elasticity models based on Hertzian contact
 171 mechanics may alternatively be applied to determine the stresses resulting from contact
 172 compression [e.g. *Herman*, 2013, 2016]. However, with nonlinear stiffness models the
 173 numerical stability of the explicit temporal integration scheme depends on the stress and
 174 packing state of the granular assemblage, and will under compressive-stress extremes re-
 175 quire very small time steps. In the simulations in this study, we use a Young's modulus of
 176 $E = 2.0 \times 10^7$ Pa. This value is lower than what is observed for ice [e.g. *Schulson*, 1999;
 177 *Petrovic*, 2003], but strikes a reasonable balance between elastic compressibility and com-
 178 putational efficiency.

179 As we demonstrate below, models based on compressive strength alone result in
 180 a weak sea-ice pack, and are not sufficient to cause granular jamming. We explore two
 181 modifications to the contact model presented in Eq. 7. The first approach is typical to
 182 DEM models and is based on resolving shear resistance through tangential (contact par-
 183 allel) elasticity, not exceeding the Coulomb frictional limit. An alternative approach, fun-
 184 damentally complementary to compressive elasticity and shear friction, is tensile strength
 185 of ice-floe contacts which leads to a cohesive bulk granular rheology.

186 2.2 Tangential elasticity with Coulomb friction

187 DEM models typically include resistance against slip between particles, by limiting
 188 relative tangential movement for inter-particle contacts [e.g. *Cundall and Strack*, 1979].

189 Tangential elasticity is resolved by determining the contact transverse travel distance δ_t
 190 (i.e. the vector of shear motion) on the contact plane for the duration of the contact t_c :

$$\delta_t^{ij} = \int_0^{t_c} \left[(\mathbf{v}^i - \mathbf{v}^j) \cdot \hat{\mathbf{t}}^{ij} - R^{ij} (\omega^i + \omega^j) \right], \quad (8)$$

191 where \mathbf{v} and ω denotes linear and angular velocity, respectively. The contact-parallel unit
 192 vector is denoted $\hat{\mathbf{t}}$. The contact transverse travel distance δ_t is corrected for contact ro-
 193 tation over the duration of the interaction, and is used to determine the contact-tangential
 194 elastic force:

$$\mathbf{f}_t^{ij} = \frac{E^{ij} A^{ij}}{R^{ij}} \frac{2(1 - (\nu^{ij})^2)}{(2 - \nu^{ij})(1 + \nu^{ij})} \delta_t^{ij}, \quad (9)$$

195 with ν^{ij} is the harmonic mean of the Poisson's ratios set for the ice floes. We use a con-
 196 stant value of $\nu = 0.185$ [Hopkins, 2004]. Coulomb friction on the grain surface limits the
 197 tangential force, relative to the magnitude of the normal force:

$$|\mathbf{f}_t^{ij}| \leq \mu^{ij} |\mathbf{f}_n^{ij}|. \quad (10)$$

198 The Coulomb-frictional coefficient μ introduced above describes resistance to sliding along
 199 the individual *grain surfaces*, and should not be mistaken for the *bulk* Mohr-Coulomb fric-
 200 tional coefficient μ_u (Eq. 2) that describes frictional behavior of an assemblage of many
 201 grains. In the case of slip ($|\mathbf{f}_t| > \mu |\mathbf{f}_n|$) the length of the contact transverse travel distance
 202 δ_t reduces to be consistent with the Coulomb limit. This loss in energy storage accounts
 203 for tangential contact plasticity and irreversible work associated with contact sliding. Since
 204 the above model of tangential shear resistance is based on deformation distance on the
 205 inter-floe contact plane, it requires solving for ice-floe rotational kinematics of each ice
 206 floe and a bookkeeping algorithm for storing contact histories.

207 **2.3 Tensile contact strength**

208 Cohesion (mechanical attraction between separating ice floes) is introduced by pa-
 209 rameterizing resistance to extension beyond the overlap distance between a pair of ice
 210 floes (i.e. $\delta_n^{ij} > 0$). For actual ice floes, tensile strength can arise due to refreezing [e.g.
 211 Menge and Jones, 1993; Schulson, 2001]. The general description of bond mechanics in-
 212 cludes resistance to bond compression, tension, shear, twist, and rolling [e.g. Potyondy and
 213 Cundall, 2004; Obermayr et al., 2013; Herman, 2016]. Here we explore the applicability
 214 of using bond resistance to *compression* and *tension* alone as mechanical components con-
 215 tributing to bulk granular shear strength. The calculations for doing so are simpler than
 216 for the elastic-plastic Coulomb friction described above.

217 We parameterize tensile strength by applying Eq. 7 for the extensive regime ($\delta_n >$
 218 0). Eq. 7 is enforced until the tensile stress exceeds the tensile strength σ_c defined for the
 219 bonds:

$$|\mathbf{f}_n^{ij}| \leq \min(\sigma_c^i, \sigma_c^j) A^{ij}. \quad (11)$$

220 Cross-sectional area of the contact is found as $A^{ij} = R^{ij} \min(h^i, h^j)$ as in Eq. 7. The bond
 221 failure corresponds to *Herman* [2016] where a complete loss of tensile stress occurs when
 222 the tensile strength is exceeded. This is different from the linear decrease in stress after
 223 failure parameterized in *Hopkins* [2004] and *Hopkins and Thorndike* [2006].

224 *Hopkins* [2004] establishes full tensile strength for the ice pack once every 24 hour
 225 cycle. Here we set the bonds to obtain full tensile strength as soon as a pair of ice floes
 226 first undergo compression ($\delta_n < 0$). Time-dependent strengthening ($\sigma_c(t)$ and $d\sigma_c/dt > 0$)
 227 causes a strain-rate weakening that is not of immediate interest for this study.

2.4 Drag from ocean and atmosphere

228 We adapt v^2 -type parameterizations for characterizing Stokes drag forces between
 229 ice floes and ocean or atmosphere. This approach is common in both Lagrangian and Eu-
 230 lerian models [e.g. *Hopkins*, 2004; *Herman*, 2016; *Rallabandi et al.*, 2017a],

$$\mathbf{f}_o^i = \pi \rho_o \left(c_{v,o} 2r^i D^i + c_{h,o} (r^i)^2 \right) (\mathbf{v}_o - \mathbf{v}^i) |\mathbf{v}_o - \mathbf{v}^i|, \quad (12)$$

232 where we use an idealized value of $\rho_o = 1 \times 10^3 \text{ kg m}^{-3}$ as ocean density, D is the ice-floe
 233 draft (here set to $D^i = 9h^i/10$), and $c_{v,o} = 0.14$ and $c_{h,o} = 1.6 \times 10^{-4}$ are vertical and hori-
 234 zontal drag coefficients [e.g. *Gladstone et al.*, 2001; *Martin and Adcroft*, 2010], compatible
 235 with typical values in sea-ice modeling [e.g. *Hopkins*, 2004]. The ocean velocity is \mathbf{v}_o and
 236 ice-floe velocity is \mathbf{v} . Similarly, for the atmosphere-induced drag:

$$\mathbf{f}_a^i = \pi \rho_a \left(c_{v,a} 2r^i (h^i - D^i) + c_{h,a} (r^i)^2 \right) (\mathbf{v}_a - \mathbf{v}^i) |\mathbf{v}_a - \mathbf{v}^i|. \quad (13)$$

237 The atmosphere density is $\rho_a = 1.3 \text{ kg m}^{-3}$. The vertical and horizontal drag coefficients
 238 are $c_{v,a} = 0.064$ and $c_{h,a} = 8.0 \times 10^{-5}$, respectively. The wind velocity is \mathbf{v}_a . The curl of
 239 the ocean or atmosphere velocities ($\nabla \times \mathbf{v}_f$) induces a rotational torque (t) on the ice floes
 240 [e.g. *Nakayama and Boucher*, 1998], sometimes ignored in DEM sea-ice models:

$$t_o^i = \pi (r^i)^4 \rho_o \left(\frac{r^i}{5} c_{h,o} + D^i c_{v,o} \right) ((\nabla \times \mathbf{v}_o)/2 - \omega^i) |(\nabla \times \mathbf{v}_o)/2 - \omega^i|, \quad (14)$$

241 and

$$t_a^i = \pi (r^i)^4 \rho_a \left(\frac{r^i}{5} c_{h,a} + (h^i - D^i) c_{v,a} \right) ((\nabla \times \mathbf{v}_a)/2 - \omega^i) |(\nabla \times \mathbf{v}_a)/2 - \omega^i|, \quad (15)$$

242 where ω is the ice-floe angular velocity. The above terms add rotational drag for a spin-
 243 ning ice floe, and can induce rotation for ice floes in ocean or atmosphere fields with high
 244 vorticity. Ocean and atmosphere curl may be reasonable to neglect on the ice-floe scale
 245 [e.g. *Herman, 2016*], but are included here nonetheless.

246 **2.5 Boundary conditions**

247 The domain boundaries can interact with the granular assemblage in a variety of
 248 ways. Ice floes are disabled from mechanical interaction with the rest of the ice floes
 249 when crossing an *inactive boundary*. Ice floes can interact mechanically across opposite
 250 sides of the model domain if the edges are *periodic boundaries*, and are immediately re-
 251 positioned to the opposite side if they cross a domain edge. *Fixed boundaries* are created by
 252 placing ice floes along a line and keeping them fixed in space. Optionally, the fixed grains
 253 can move at prescribed velocities. The free-moving ice floes undergo the same mechanical
 254 interactions with the fixed ice floes as used for their internal interactions. For the cohesive
 255 model tensile bonds between free and fixed ice floes effectively create landfast ice areas.
 256 Finally, flat and frictionless walls can provide *normal stress boundaries* to the granular as-
 257 semblage. These walls attempt to fulfill a certain contact stress normal to their geometric
 258 orientation, and move through time to uphold the prescribed stress. They are assigned a
 259 constant mass, and their kinematics are resolved with explicit temporal integration of their
 260 stress balance, similar to the temporal integration performed for the ice floes themselves.

261 **2.6 Model limitations**

262 The presented model is not sufficiently general for being a complete formulation for
 263 sea-ice mechanics. For example, we do not include a parameterization of pressure ridging,
 264 important for mechanical redistribution of ice mass in converging regimes [e.g. *Thorndike*
 265 *et al.*, 1975; *Rothrock*, 1975; *Hibler*, 1980; *Hopkins et al.*, 1991; *Flato and Hibler*, 1995;
 266 *Lipscomb et al.*, 2007]. Furthermore, the ice floe shape is highly simplified as we neglect
 267 geometrical anisotropy and associated mechanical effects [e.g. *Hopkins*, 2004; *Wilchin-*
 268 *sky and Feltham*, 2006; *Feltham*, 2008; *Wilchinsky et al.*, 2011]. However, direct modeling
 269 of polygonal sea-ice floes is computationally excessive in the targeted context. Here we
 270 focus on differences between simple DEM models with the fewest additional layers of ab-
 271 straction. Consequentially, the simulation results should not be compared directly to real
 272 settings, as further analysis and model development is required to do so.

273 The components of interaction on the ice-floe scale influence the bulk behavior un-
274 der various settings and forcings. The interaction described in the previous is typical for
275 DEM implementations for sea ice in the literature [e.g. *Hopkins*, 1996, 2004; *Herman*,
276 2016].

277 **3 Numerical model**

278 **3.1 Implementation**

279 We implement the model described above as a stand-alone and purpose-built DEM
280 sea-ice model `Granular.jl` [*Damsgaard*, 2018a]. In this study we use drag from pre-
281 scribed ocean and atmosphere velocity fields, and explore strengths and limitations of
282 different methods related to sea-ice mechanics. A separate online repository contains the
283 simulation scripts [*Damsgaard*, 2018b].

284 The effects of the ocean and atmosphere are here prescribed as constant velocity
285 fields. The interpolation to the discrete ice floes is determined with bilinear interpolation
286 to the ocean and atmosphere grids. The relative importance of neighboring grid points de-
287 creases linearly with distance. Ice-floe contacts are detected by binning the population of
288 ice floes within a grid, where the cell width equals the largest ice floe diameter. All con-
289 tacts for an ice floe can reliably be detected by searching for overlaps within the current
290 and eight neighboring cells. Ice floes are transferred between the cell lists according to
291 their movement through the sorting grid. This approach significantly reduces the computa-
292 tional overhead ($O(n)$) compared to all-to-all contact searches ($O(n^2)$) [e.g. *Ericson*, 2005].
293 We do not include thermodynamic processes and ice-floe geometries do not change over
294 the course of each simulation.

295 **3.2 Experiments**

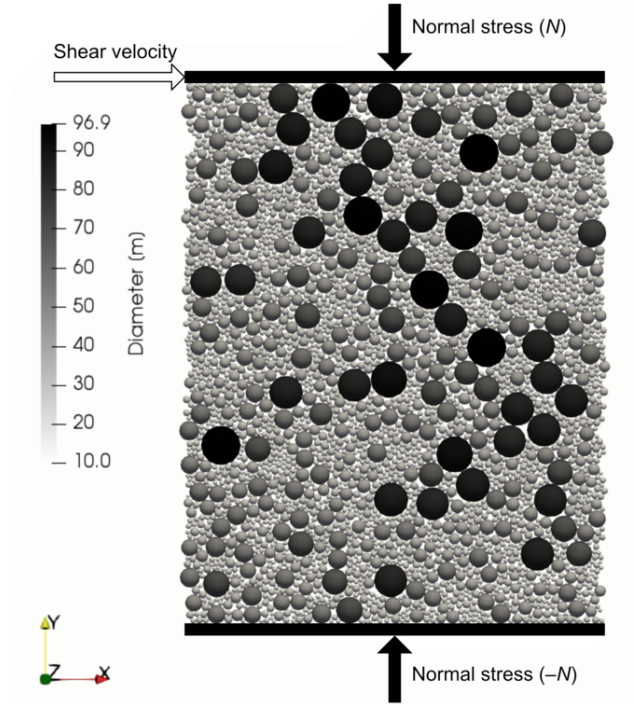
296 We perform two types of experiments in order to understand the granular rheology
297 and its applicability to simulate sea-ice dynamics. In both cases we generate ice-floe sizes
298 by a power-law distribution within the range r_{\min} to r_{\max} with an exponent of value -1.8 ,
299 commonly used for describing sea ice in the marginal zone [e.g. *Steer et al.*, 2008; *Her-*
300 *man*, 2010, 2013]. For the experiments we parameterize the granular interaction in one of
301 two ways:

- 302 1. **Coulomb-frictional DEM:** Linear-elastic resistance to compressive strain normal
 303 to the contact interface (Eq. 7) and linear-elastic resistance to shear strain on the
 304 contact interface, with Coulomb friction limiting the tangential force magnitude
 305 (Eq. 10). The kinematics are resolved with the translational and rotational momen-
 306 tum equations (Eqs. 5 and 6).
- 307 2. **Cohesive DEM:** Linear-elastic resistance to compressive strain normal to the con-
 308 tact interface (Eq. 7) and linear-elastic resistance to extensional strain between a
 309 bonded ice-floe pair with a breakage criterion (Eq. 11). The kinematics are re-
 310 solved for translation only (Eq. 5). Rotation (Eq. 6) and contributing components
 311 (Eqs. 8, 9, 10, and 14–15) are ignored.

312 Approach (1) requires that rotational kinematics of the ice floes are resolved (Eq. 6) for
 313 correctly determining the tangential contact displacement (Eq. 8). Including rotation ap-
 314 proximately doubles the kinematic degrees of freedom and required computations. Ap-
 315 proach (2) is computationally cheaper as it does not require resolving rotation (the ice
 316 floes are effectively frictionless). Without friction, the bulk shear strength is provided
 317 by geometrical roughness in the granular contact network. Cohesion further strengthens
 318 the granular topology and adds increased bulk resistance to deformation. The Coulomb-
 319 frictional model (approach 1) is the standard method for simulating cohesionless granular
 320 materials, and will for our purposes serve as a benchmark for testing the applicability of
 321 the less complex cohesive model (approach 2). We expect that the bulk mechanics for the
 322 two models can be similar in certain settings, but differ in others as the micromechanical
 323 behavior is fundamentally different.

324 3.2.1 *Simple shear*

325 We perform simple shear experiments on dense granular packings, where the ice
 326 floes are sheared from a pre-consolidated state under a constant normal stress (Fig. 1).
 327 The primary objective of these experiments is to validate the Mohr-Coulomb frictional be-
 328 havior typical for granular materials (Eq. 2) [e.g. *Nedderman, 1992*], and assess how the
 329 type of grain-to-grain contact rheology influences bulk stress properties. In the shear ex-
 330 periments we do not include ocean and atmosphere drag, as we are interested in analyzing
 331 the ice-floe mechanics alone.



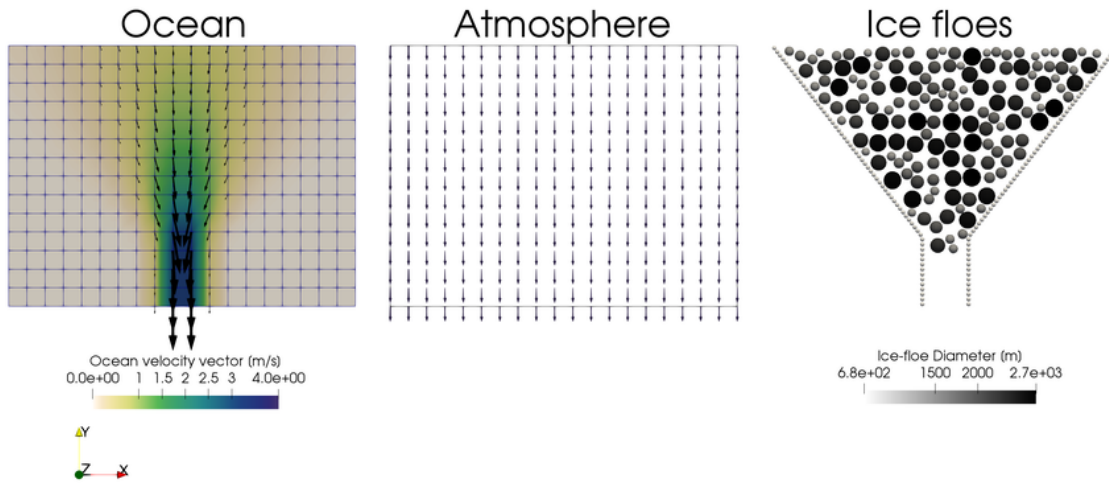
332 **Figure 1.** Simulation setup for the simple shear experiments. The upper and lower walls exert a prescribed
 333 normal stress to the granular assemblage, and a constant velocity along x is enforced for the uppermost ice
 334 floes. Left and right ($-x$ and $+x$) boundaries are periodic.

335 We adapt a simple-shear setup with boundary conditions typical in DEM modeling
 336 [e.g. *Damsgaard et al., 2013*], with a schematic overview in Figure 1. We initially gen-
 337 erate ice floes with radii between 5 and 50 m in an irregular spatial arrangement without
 338 geometrical overlaps. We then apply a uniform ocean drag towards the lower boundary
 339 ($-y$) in order to increase the packing ratio. We then disable the ocean drag and perform a
 340 *consolidation step* in order to further uniaxially compress the packing in equilibrium with
 341 the stress forcing, as common in Mohr-Coulomb tests on granular materials [e.g. *Bowles,*
 342 *1992; Mitchell and Soga, 2005*]. The consolidation is performed by adding a normal stress
 343 boundary condition to the top ($+y$). Finally, we perform a constant-rate *shear step* by
 344 prescribing a velocity towards $+x$ of 1 m s^{-1} to the grains just below the upper bound-
 345 ary (Fig. 1). The bulk shear stress is determined from the sum of contact forces along y
 346 against the top grains. The side boundaries ($-x$ and $+x$) are periodic in order allow arbi-
 347 trary shear strains without geometrical constraints. Grains that are positioned within one
 348 grain size to the lower boundary ($-y$) are fixed in space in order to provide geometrical
 349 and mechanical roughness. The parameter choices result in granular inertia parameters in

350 the range of $I = [10^{-3}; 10^{-2}]$ (Eq. 3), so slight shear-rate dependence on the observed bulk
 351 shear stress can be expected.

3.2.2 Jamming in idealized straits

352
 353 In this set of experiments we use ocean and atmosphere drag to push the ice floes
 354 through a confining strait of funnel-shaped geometry (Fig. 2), and analyze how the ice-
 355 floe properties influences the likelihood of granular jamming. The geometry is similar to
 356 ones from earlier studies focused on ice-discharge with smoothed particle dynamics and a
 357 discrete element model outside of the regime of granular jamming [Gutfraind and Savage,
 358 1998]. The ice floes are forced with wind and ocean current fields oriented from north to
 359 south. The spatial velocity pattern of the ocean is defined by a stream function, where the
 360 ocean flows through the confining strait with a velocity field consistent with mass conser-
 361 vation. Ice floes are initially placed in a pseudo-random arrangement north of the channel.
 362 During our initial tests we observed that the simulated material never jammed *inside* the
 363 flat-walled channel, but always at or before the channel entrance. For that reason, we con-
 364 strain our simulation domain size to only include the relevant parts.



365 **Figure 2.** Simulation setup for the idealized strait experiments. Ocean velocities vary from 0 to 4 m/s
 366 relative to the bounding geometry, while the atmosphere velocity field is a uniform value of 30 m/s.

367 New ice floes are continuously added to the top of the domain as soon as there is
 368 space to accommodate them. The sizes are drawn from the same power-law size distri-
 369 bution. The bottom edge of the domain is an inactive boundary. During each experiment

370 we determine the mass of disabled ice floes at the bottom as a measure of cumulative ice
 371 transport through the strait. If granular jamming occurs, ice floes stop reaching the bot-
 372 tom. We impose the criteria that the ice mass at the bottom must have been constant for
 373 more than one hour in simulation time for being classified as jammed. The experiments
 374 rely on pseudo-random number generation (pRNG) for generating ice-floe size distribu-
 375 tions, in order to obtain statistical description of the behavior (Eq. 1). The radii are drawn
 376 between 600 and 1350 m. We seed the pRNG with different values and repeat each exper-
 377 iment ten times with identical mechanical parameters to assess the statistical probability of
 378 granular jamming.

379 **4 Results**

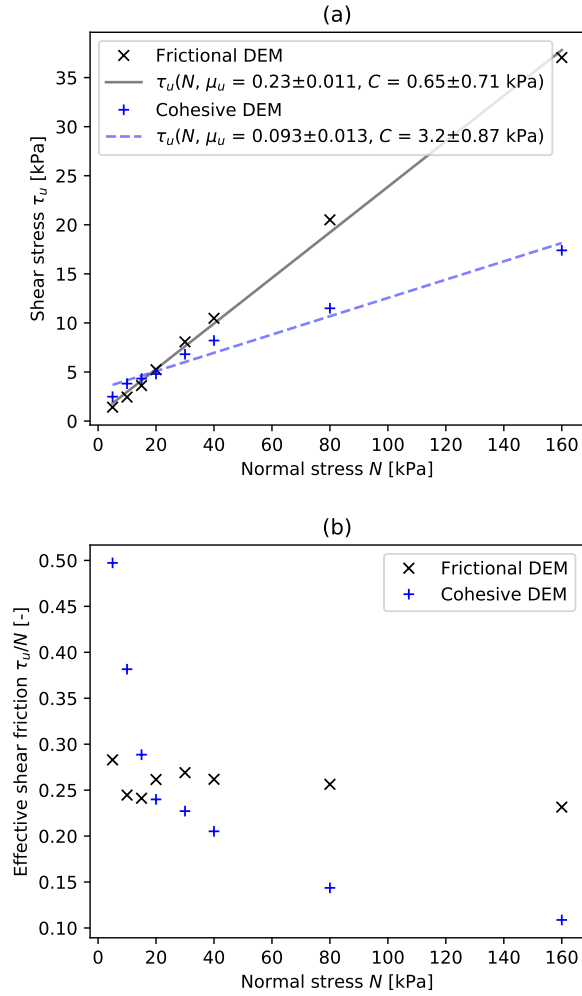
380 In this section we compare bulk behavior between the algorithmically complex Coulomb-
 381 frictional model and the simpler cohesive model. The supplementary material contains
 382 animations of the shear and jamming experiments.

383 A benchmark of the computational performance reveals that the interaction routine is
 384 $2.1\times$ faster for the cohesive model relative to the Coulomb-frictional model. By avoiding
 385 rotation, kinematic degrees of freedom are in our 2d setup reduced from 9 to 6 for the
 386 cohesive model. The models have identical requirements for the granular contact search,
 387 so performance here is not improved.

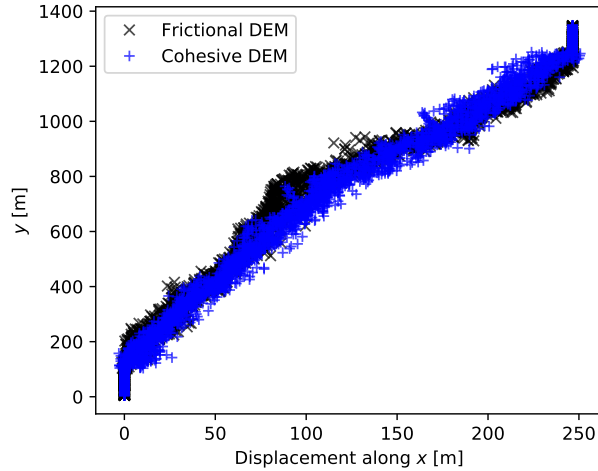
394 **4.1 Simple shear**

395 We observe that both the Coulomb-frictional and cohesive models follow the Mohr-
 396 Coulomb constitutive relation (Eq. 2), as the bulk shear stress of the granular assemblages
 397 τ_u scales linearly with normal stress N applied normal to the shear direction (Fig. 3a).
 398 The Coulomb-frictional model produces an ice-floe pack with a small value for bulk co-
 399hesion (C) and a strong linear correlation between normal stress and shear stress. The
 400 cohesive model results in an ice-floe pack with a higher bulk cohesion, but it also shows
 401 increasing shear stresses with increasing normal stress. There is a reasonable overlap in
 402 shear stress between the two models at $N \in [5; 40]$ kPa. However, the bulk friction is not
 403 the same across a larger range of N because of the micromechanical differences.

404 The effective shear friction (τ_u/N) is a metric that describes bulk mechanical prop-
 405 erties during shear (Fig. 3b). For the Coulomb-frictional tests, we see that the bulk fric-



388 **Figure 3.** Steady-state stress and friction during simple shear for Coulomb-frictional model runs ($\mu = 0.3$
 389 and $\sigma_c = 0$ kPa, see Eq. 10 and 11), and cohesive model runs ($\mu = 0$ and $\sigma_c = 200$ kPa). (a) The bulk shear
 390 stress τ_u increases linearly with the applied normal stress. We optimize Eq. 2 using a least-squares fit and note
 391 parameter estimates and 95% confidence intervals in the legend. (b) Effective friction observed in the two
 392 model types.

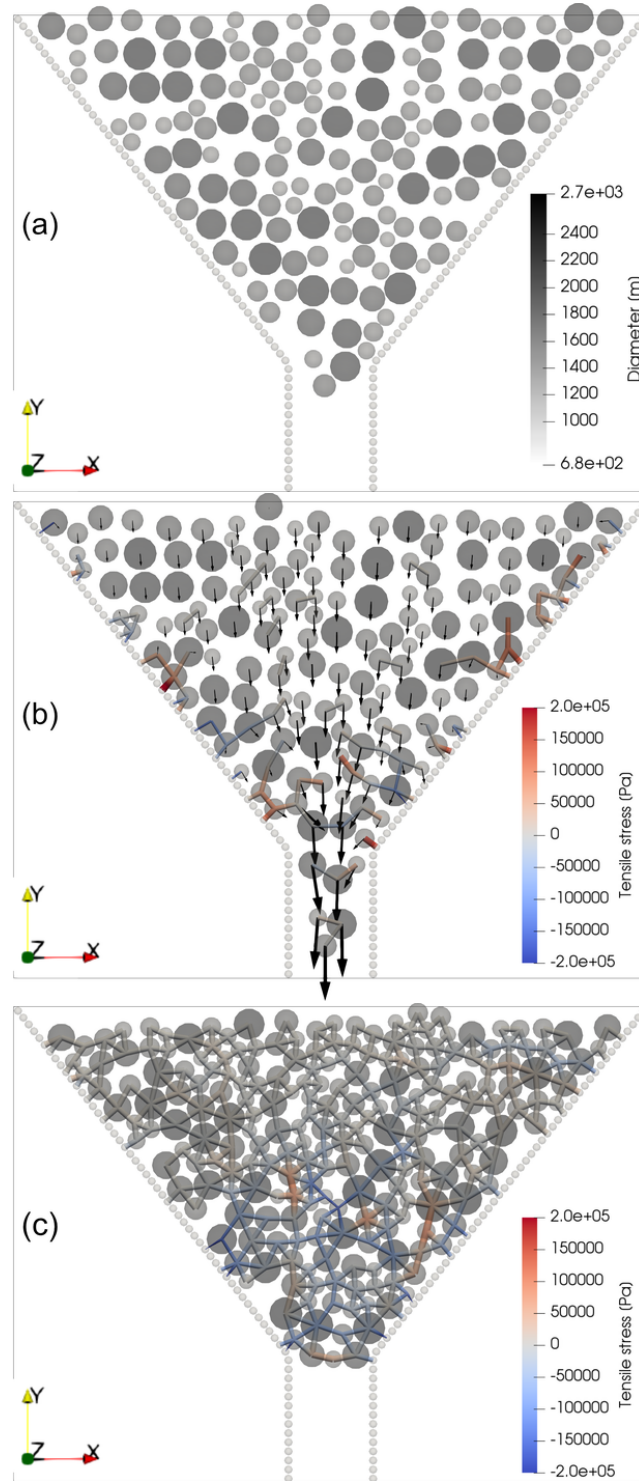


393 **Figure 4.** Ice-floe displacements in the simple shear experiments with a normal stress of $N = 20$ kPa.

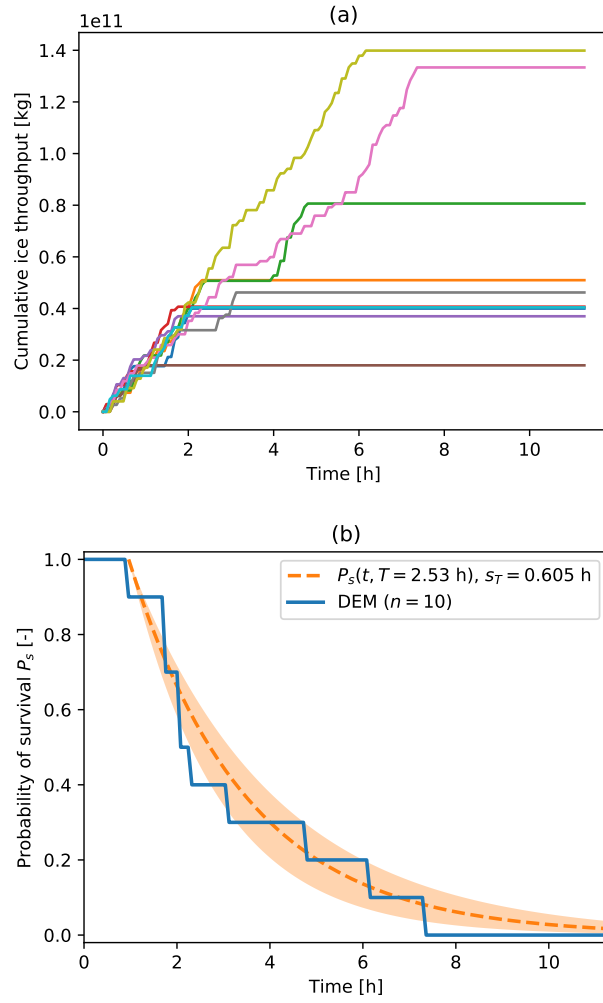
406 tional coefficient ($\mu_u \approx 0.25$, Eq. 2) is lower than the Coulomb-frictional coefficient we
 407 parameterize on the contact level ($\mu = 0.3$, Eq. 10). Ice-floe rotation decreases the bulk
 408 strength, which is common for two-dimensional granular systems with circular grains. The
 409 Coulomb-frictional model retains most of its effective friction under the tested range of
 410 normal stresses (Fig. 3b), in line with observations of sea ice mechanics [Schulson *et al.*,
 411 2006; Weiss *et al.*, 2007; Fortt and Schulson, 2007, e.g.]. In contrast, the cohesive model
 412 becomes monotonically weaker under larger normal stresses, with a large decrease in the
 413 lower range of N . While strong cohesion is expected to localize failure the distribution of
 414 shear strain (Fig. 4) is similar in the two models. The only difference is that shear strain is
 415 slightly more localized towards the moving boundary in the Coulomb-frictional DEM, and
 416 more linear and distributed in the cohesive DEM.

417 **4.2 Jamming in idealized straits**

427 By adjusting the grain-to-grain frictional coefficient μ (Eq. 10) and the tensile strength
 428 σ_c (Eq. 11) we can assess jamming tendencies in the two models. Figure 6a shows that
 429 the time to jamming is strongly influenced by small variations in initial ice-floe configu-
 430 rations. With the applied contact parameters ($\mu = 0$ and $\sigma_c = 400$ kPa), all ten runs jam
 431 after a period of ~ 7 hours. We plot the ratio of survived (non-jammed) runs as a func-
 432 tion of time (Fig. 6b), and fit an exponential decay function to the survival fraction [Eq. 1,
 433 Tang *et al.*, 2009] with the Levenberg-Marquardt algorithm of nonlinear least squares op-

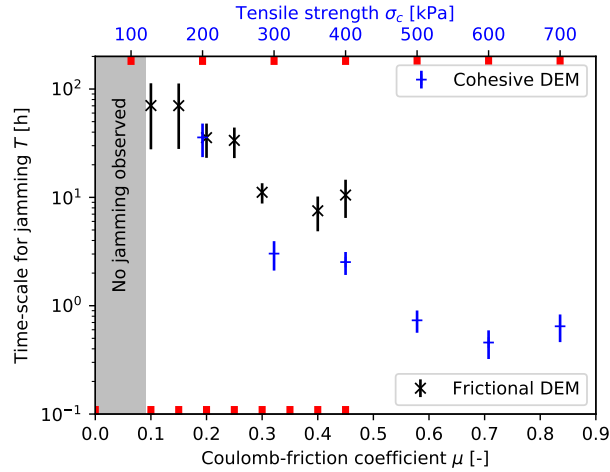


418 **Figure 5.** Example visualization of the granular system for the *idealized strait* runs, here the initial state (a),
 419 during flow (b), and in a jammed state (c). Black arrows denote the linear velocity of the ice floes, and colored
 420 bars indicate compressive or tensile granular interactions. The above visualizations are for run one out of ten
 421 with $\mu = 0$ and $\sigma_c = 400$ kPa.



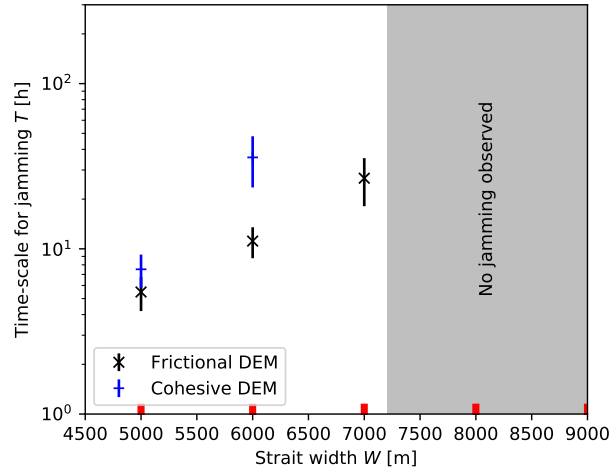
422 **Figure 6.** (a) The cumulative mass of ice flushed through the idealized strait over time in experiments of
 423 identical mechanical parameters (cohesive model, $\mu = 0$ and $\sigma_c = 400$ kPa), but with random perturbations
 424 to the initial ice-floe placements and sizes. (b) Probability of survival (non-jamming) P_s for the ensemble in
 425 (a), with a corresponding least-square fit of Eq. 1. The legend shows the best-fit value for the characteristic
 426 jamming time T , as well as the sample standard deviation around the mean.

434 timization. The decay time-scale parameter T and the sample standard deviation s_T are
 435 useful metrics for comparing the effect of different prescribed properties to the jamming
 436 behavior of the ice-pack system. We offset the curve fit in time corresponding to the first
 437 occurrence of jamming.



438 **Figure 7.** The influence of the Coulomb-frictional coefficient μ (Eq. 10) and the tensile strength σ_c
 439 (Eq. 11) on the characteristic time for jamming T (Eq. 1) through a strait of width $W = 6000$ m. A statisti-
 440 cally significant fit could not be achieved from the Coulomb-frictional ensemble with $\mu = 0.35$. Red ticks
 441 denote tested values.

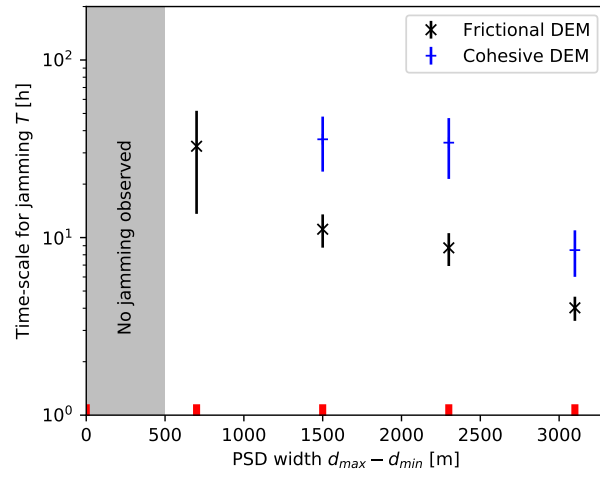
442 We observe that larger friction coefficients μ increase the mechanical rigidity and
 443 increase the likelihood of jamming in the Coulomb-frictional model with rotation (Fig. 7,
 444 black ticks). Similarly, increases in grain-to-grain tensile strength increases the likelihood
 445 of jamming in the reduced-complexity model with cohesion (Fig. 7, blue ticks). Neither
 446 model displays jamming as the system becomes frictionless ($\mu \rightarrow 0$) or cohesionless
 447 ($\sigma_c \rightarrow 0$), highlighting the need for including interactions other than contact-normal elastic
 448 repulsion (Eq. 7). Due to the monotonic nature of the jamming timescale in both models,
 449 we can determine a value for the tensile strength σ_c that with the cohesive model corre-
 450 sponds to the jamming behavior of a certain μ value for the Coulomb-frictional model (or
 451 vice versa). The jamming behavior is broadly similar for the Coulomb-frictional model
 452 with $\mu = 0.3$ and $\sigma_c = 0$ kPa, and the cohesive model with $\mu = 0$ and $\sigma_c = 200$ kPa
 453 (Fig. 7a,b).



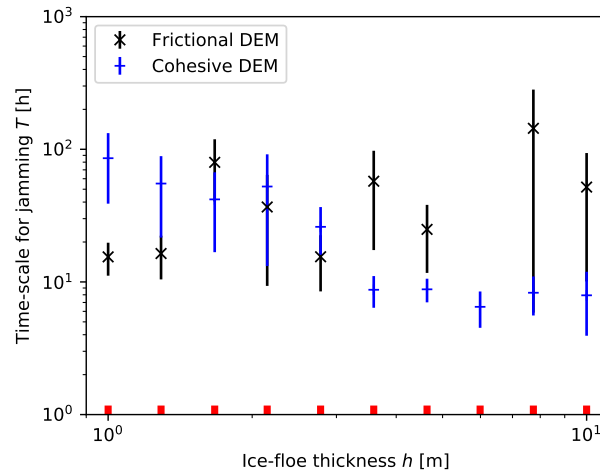
454 **Figure 8.** Jamming behavior with increasing width of the strait (Fig. 5) for Coulomb-frictional ($\mu = 0.3$ and
 455 $\sigma_c = 0$ kPa) and cohesive runs ($\mu = 0$ and $\sigma_c = 200$ kPa). The frictional model does not show jamming above
 456 $W = 7000$ m, and the cohesive model does not show jamming above $W = 6000$ m. Red ticks denote tested
 457 values.

458 In both models, jamming does not occur across straits that are wide with respect
 459 to grain size, consistent with the expectation of constant granular discharge across wide
 460 confinements (Fig. 8). As strait width decreases, the jamming timescale T decreases in a
 461 nonlinear fashion for both the Coulomb-frictional and cohesive models. With the applied
 462 parameters the Coulomb-frictional model was able to jam in straits of width $W = 7000$ m,
 463 while the cohesive model only displayed jamming up to $W = 6000$ m.

464 We also increase the width of the generated particle-size distribution (PSD) around
 465 the same mean value, and observe that jamming occurs faster in wide size spans (Fig. 9).
 466 While smaller ice floes act as lubricants facilitating flow, larger ice floes provide structural
 467 rigidity leading to eventual jamming. It is primarily the advection of larger ice floes to
 468 the strait entrance that cause the jamming itself. In the Coulomb-frictional model, ice-floe
 469 thickness does not directly influence jamming behavior (Fig. 10), as the presented imple-
 470 mentation adjusts stress-based yield criteria for contact sliding and tensile bond breakage
 471 accordingly. However, the cohesive model displays increased likelihood of jamming with
 472 increased thicknesses, similar to previous studies of ice-bridge stability in confinements
 473 [Rallabandi *et al.*, 2017b].



474 **Figure 9.** Jamming behavior with increasing width of the particle-size distribution for Coulomb-frictional
 475 ($\mu = 0.3$ and $\sigma_c = 0$ kPa) and cohesive runs ($\mu = 0$ and $\sigma_c = 200$ kPa). Red ticks denote tested values.



476 **Figure 10.** Jamming behavior with uniformly increasing thickness of the ice floes for Coulomb-frictional (μ
 477 = 0.3 and $\sigma_c = 0$ kPa) and cohesive runs ($\mu = 0$ and $\sigma_c = 200$ kPa). Red ticks denote tested values.

5 Discussion and Summary

We have developed a flexible discrete-element framework for simulating Lagrangian sea-ice dynamics at the ice-floe scale, forced by ocean and atmosphere velocity fields. Frictionless contact models based on compressive stiffness alone are very unlikely to jam. We describe two different approaches based on Coulomb friction and tensile strength, where both additions result in increased bulk shear strength of the granular assemblage. We demonstrate that the discrete-element approach is able to undergo granular jamming when forced through an idealized confinement, where the probability of jamming is determined by the channel width, ice-floe thicknesses, and ice-floe size variability. The frictionless but cohesive contact model can with certain tensile strength values display jamming behavior which on the large scale is broadly similar to a model with contact friction and ice-floe rotation. However, the behavior of the two models is not exactly similar in other settings. During shear the models show separate trends in bulk effective friction, and differing behavior is expected under pure divergent forcings.

Our results are consistent with previous studies on granular mechanics, specifically regarding how the magnitude of the Coulomb-frictional coefficient influences bulk behavior. *Morgan* [1999] demonstrated that the particle-frictional coefficient increases bulk frictional strength of dense and two-dimensional systems up to a certain point where grain rolling becomes dominant over grain-to-grain contact sliding. *Kamrin and Koval* [2014] showed that particle-surface friction effects bulk behavior, and that increasing Coulomb-frictional coefficients increase shear strength. Furthermore, and under certain conditions, the spatial distribution of shear deformation can be affected by the micro-mechanical grain friction. *Morgan* [2015] investigated the combined effects of Coulomb friction and tensile cohesion on the structural and mechanical evolution of fold and thrust belts and contractional wedges. In this study, broken bonds did not reform over time. It was observed that large tensile bond strengths caused increases in bulk shear strength, primarily by increasing the bulk cohesion in the Mohr-Coulomb constitutive relationship. Cohesion caused the material to behave in a rigid manner, with thin shear zones of broken bonds where bonds have failed. Without cohesion, deformation was more distributed in space. In our experiments, we observe similar behavior where increasing tensile strengths makes a dense ice pack behave like a rigid system (Fig. 5c). However, our parameterization reforms bonds progressively when ice floes again come into contact, which limits the strain weakening otherwise associated with bond breaking.

511 The Coulomb-frictional DEM model naturally strengthens in a linear manner with
512 increasing compressive stress on the contacts (Eq. 10), which linearly increases bulk shear
513 strength (Fig. 3a), as typical for granular materials tested in laboratory shear devices or
514 when simulated with the DEM [e.g. *Damsgaard et al.*, 2013; *Morgan*, 2015]. The contacts
515 of the cohesive model do not strengthen due to increased contact loading, which explains
516 the weaker behavior observed at large normal stresses (Fig. 3c). However, shear strength
517 does still increase, since larger normal stresses on the shear zone cause self-arrangement
518 into a denser packing. The dense system contains relatively more contacts containing ten-
519 sile strength, which on a bulk scale strengthens the mechanical resistance to shear. While
520 cohesion can affect deformation patterns [e.g. *Morgan*, 2015] the shear profiles are not
521 significantly different between the two profiles (Fig. 4). We do not expect notable differ-
522 ence in deformation patterns on larger scales unless strong cohesion is applied.

523 The approach used in this study relies on many simplifications and is not capable of
524 producing the richness of sea ice behavior observed in nature, both in terms of geometry
525 and interaction. These limitations can be removed if computational efficiency is less than
526 a central concern. Cylindrical or circular grain-shape representations slightly reduce bulk
527 shear strength relative to particles of irregular shape [e.g. *Mair et al.*, 2002]. In an attempt
528 to compensate for shape-induced weakening, the Coulomb-frictional coefficient or tensile
529 strength can be increased in order to tend to the desired bulk mechanics. Furthermore, it
530 may be beneficial to add random variation to mechanical properties (e.g., μ and σ_c), if
531 the range of variability is well understood. Ice-floe ridging is by crude means approxi-
532 mated by the bonding process described here, but it may be possible to improve the floe-
533 scale mechanics for this process [e.g. *Rothrock*, 1975; *Flato and Hibler*, 1995; *Lipscomb*
534 *et al.*, 2007], especially if thermodynamic balance and the important process of refreezing
535 is determined in conjunction with ocean and atmosphere state. Instead of attempting the
536 impossible goal of including the entire details of the complex sea-ice system, we intend
537 for this parameterization to be a useful first attempt at making Lagrangian and ice-floe
538 scale methods available for coupled and global climate models. Lagrangian formulations
539 have inherent advantages to continuum sea-ice models, especially for handling the discon-
540 tinuous behavior in shear zones and granular phenomena in the ice-marginal zone. We
541 demonstrate that simplifications in discrete-element method formulations can reduce the
542 algorithmic complexity while retaining similar shear zone morphology and jamming be-
543 havior.

544 **Acknowledgments**

545 This work was supported by ExxonMobil through its membership in the Princeton E-
546 filliates Partnership of the Andlinger Center for Energy and the Environment. Anders
547 Damsgaard benefited from discussions with Alon A. Stern, Mitchell Bushuk, Michael
548 Winton, and Behrooz Ferdowsi in preparation for this paper. We thank the reviewers and
549 associate editor for constructive criticism which has greatly improved the content of this
550 paper.

551 **References**

- 552 Aharonov, E., and D. Sparks (1999), Rigidity phase transition in granular packings, *Physical*
553 *Review E*, *60*(6), 6890–6896.
- 554 Aharonov, E., and D. Sparks (2002), Shear profiles and localization in simulations of
555 granular shear, *Phys. Rev., E*, *65*, 051,302.
- 556 Bak, P., C. Tang, and K. Wiesenfeld (1988), Self-organized criticality, *Phys. Rev. A*, *38*(1),
557 364–374, doi:10.1103/physreva.38.364.
- 558 Bouzid, M., M. Trulsson, P. Claudin, E. Clément, and B. Andreotti (2013), Nonlocal
559 rheology of granular flows across yield conditions, *Phys. Rev. Lett.*, *111*(23), doi:
560 10.1103/physrevlett.111.238301.
- 561 Bowles, J. E. (1992), *Engineering Properties of Soils and Their Measurement*, 241 pp.,
562 Irwin/McGraw-Hill.
- 563 Cates, M. E., J. P. Wittmer, J.-P. Bouchaud, and P. Claudin (1998), Jamming, force chains,
564 and fragile matter, *Phys. Rev. Lett.*, *81*(9), 1841–1844, doi:10.1103/physrevlett.81.1841.
- 565 Chiang, J. C. H., and C. M. Bitz (2005), Influence of high latitude ice cover on the marine
566 Intertropical Convergence Zone, *Clim. Dyn.*, *25*(5), 477–496, doi:10.1007/s00382-005-
567 0040-5.
- 568 Coon, M. (1974), Mechanical behavior of compacted Arctic ice floes, *J. Petr. Tech.*,
569 *26*(04), 466–470, doi:10.2118/3956-pa.
- 570 Cundall, P. A., and O. D. L. Strack (1979), A discrete numerical model for granular as-
571 semblies, *Géotechnique*, *29*, 47–65, doi:10.1680/geot.1979.29.1.47.
- 572 Curry, J. A., J. L. Schramm, and E. E. Ebert (1995), Sea ice-albedo cli-
573 mate feedback mechanism, *J. Climate*, *8*(2), 240–247, doi:10.1175/1520-
574 0442(1995)008<0240:siacfm>2.0.co;2.

- 575 da Cruz, F., S. Emam, M. Prochnow, J.-N. Roux, and F. Chevoir (2005), Rheophysics of
 576 dense granular materials: Discrete simulation of plane shear flows, *Phys. Rev. E*, *72*(2),
 577 doi:10.1103/physreve.72.021309.
- 578 Damsgaard, A. (2018a), Granular.jl: Julia package for granular dynamics simulation, Ver-
 579 sion 0.3.2, doi:10.5281/zenodo.1165990.
- 580 Damsgaard, A. (2018b), SealIce-experiments: Simulation scripts using Granular.jl, Version
 581 1.0.0, doi:10.5281/zenodo.1166005.
- 582 Damsgaard, A., D. L. Egholm, J. A. Piotrowski, S. Tulaczyk, N. K. Larsen, and K. Tyl-
 583 mann (2013), Discrete element modeling of subglacial sediment deformation, *J. Geo-
 584 phys. Res. Earth Surf.*, *118*, 2230–2242, doi:10.1002/2013JF002830.
- 585 Damsgaard, A., D. L. Egholm, L. H. Beem, S. Tulaczyk, N. K. Larsen, J. A. Piotrowski,
 586 and M. R. Siegfried (2016), Ice flow dynamics forced by water pressure variations in
 587 subglacial granular beds, *Geophys. Res. Lett.*, *43*, doi:10.1002/2016gl071579.
- 588 Damsgaard, A., A. Cabrales-Vargas, J. Suckale, and L. Goren (2017), The coupled dy-
 589 namics of meltwater percolation and granular deformation in the sediment layer un-
 590 derlying parts of the big ice sheets, in *Poromechanics VI*, Am. Soc. Civ. Eng., doi:
 591 10.1061/9780784480779.024.
- 592 de Borst, R. (1991), Numerical modelling of bifurcation and localisation in cohesive-
 593 frictional materials, *Pure Appl. Geophys.*, *137*(4), 367–390.
- 594 Delworth, T. L., A. J. Broccoli, A. Rosati, R. J. Stouffer, V. Balaji, J. A. Beesley, W. F.
 595 Cooke, K. W. Dixon, J. Dunne, K. Dunne, et al. (2006), GFDL's CM2 global coupled
 596 climate models. part I: Formulation and simulation characteristics, *J. Climate*, *19*(5),
 597 643–674.
- 598 Deser, C., J. E. Walsh, and M. S. Timlin (2000), Arctic sea ice variability in the context
 599 of recent atmospheric circulation trends, *J. Climate*, *13*(3), 617–633, doi:10.1175/1520-
 600 0442(2000)013<0617:asivit>2.0.co;2.
- 601 Ergenzinger, C., R. Seifried, and P. Eberhard (2011), A discrete element model to de-
 602 scribe failure of strong rock in uniaxial compression, *Granul. Matter*, *13*, 341–364, doi:
 603 10.1007/s10035-010-0230-7.
- 604 Ericson, C. (2005), *Real-Time Collision Detection*, 413–426 pp., Morgan Kauf-
 605 mann/Elsevier, San Diego, CA, doi:10.1016/b978-1-55860-732-3.50015-2.
- 606 Feltham, D. L. (2005), Granular flow in the marginal ice zone, *Phil. Trans. R. Soc. A*,
 607 *363*(1832), 1677–1700, doi:10.1098/rsta.2005.1601.

- 608 Feltham, D. L. (2008), Sea ice rheology, *Ann. Rev. Fluid Mech.*, *40*(1), 91–112, doi:
 609 10.1146/annurev.fluid.40.111406.102151.
- 610 Flato, G. M., and W. D. Hibler (1995), Ridging and strength in modeling the thickness
 611 distribution of Arctic sea ice, *J. Geophys. Res.*, *100*(C9), 18,611, doi:10.1029/95jc02091.
- 612 Forterre, Y., and O. Pouliquen (2008), Flows of dense granular media, *Ann. Rev. Fluid
 613 Mech.*, *40*(1), 1–24, doi:10.1146/annurev.fluid.40.111406.102142.
- 614 Fortt, A. L., and E. M. Schulson (2007), The resistance to sliding along Coulombic shear
 615 faults in ice, *Acta Mat.*, *55*(7), 2253–2264, doi:10.1016/j.actamat.2006.11.022.
- 616 Fortt, A. L., and E. M. Schulson (2009), Velocity-dependent friction on coulombic shear
 617 faults in ice, *Acta Mat.*, *57*(15), 4382–4390, doi:10.1016/j.actamat.2009.06.001.
- 618 GDR-MiDi (2004), On dense granular flows, *Eur. Phys. J. E*, *14*, 341–365, doi:
 619 10.1140/epje/i2003-10153-0.
- 620 Girard, L., J. Weiss, J. M. Molines, B. Barnier, and S. Bouillon (2009), Evaluation of
 621 high-resolution sea ice models on the basis of statistical and scaling properties of Arctic
 622 sea ice drift and deformation, *J. Geophys. Res.*, *114*(C8), doi:10.1029/2008jc005182.
- 623 Girard, L., S. Bouillon, J. Weiss, D. Amitrano, T. Fichefet, and V. Legat (2011), A new
 624 modeling framework for sea-ice mechanics based on elasto-brittle rheology, *Ann.
 625 Glaciol.*, *52*(57), 123–132, doi:10.3189/172756411795931499.
- 626 Gladstone, R. M., G. R. Bigg, and K. W. Nicholls (2001), Iceberg trajectory modeling and
 627 meltwater injection in the Southern Ocean, *J. Geophys. Res.: Oceans*, *106*(C9), 19,903–
 628 19,915, doi:10.1029/2000jc000347.
- 629 Gnanadesikan, A., K. W. Dixon, S. M. Griffies, V. Balaji, M. Barreiro, J. A. Beesley,
 630 W. F. Cooke, T. L. Delworth, R. Gerdes, M. J. Harrison, I. M. Held, W. J. Hurlin, H.-
 631 C. Lee, Z. Liang, G. Nong, R. C. Pacanowski, A. Rosati, J. Russell, B. L. Samuels,
 632 Q. Song, M. J. Spelman, R. J. Stouffer, C. O. Sweeney, G. Vecchi, M. Winton, A. T.
 633 Wittenberg, F. Zeng, R. Zhang, and J. P. Dunne (2006), GFDL's CM2 global coupled
 634 climate models. part II: The baseline ocean simulation, *J. Climate*, *19*(5), 675–697, doi:
 635 10.1175/jcli3630.1.
- 636 Griffies, S. M., A. Gnanadesikan, K. W. Dixon, J. P. Dunne, R. Gerdes, M. J. Harrison,
 637 A. Rosati, J. L. Russell, B. L. Samuels, M. J. Spelman, M. Winton, and R. Zhang
 638 (2005), Formulation of an ocean model for global climate simulations, *Ocean Sci.*, *1*(1),
 639 45–79, doi:10.5194/os-1-45-2005.

- 640 Gutfraind, R., and S. B. Savage (1997a), Marginal ice zone rheology: Comparison of re-
 641 sults from continuum-plastic models and discrete-particle simulations, *J. Geophys. Res.:
 642 Oceans*, *102*(C6), 12,647–12,661, doi:10.1029/97jc00124.
- 643 Gutfraind, R., and S. B. Savage (1997b), Smoothed particle hydrodynamics for the simula-
 644 tion of broken-ice fields: Mohr–Coulomb-type rheology and frictional boundary condi-
 645 tions, *J. Comput. Phys.*, *134*(2), 203–215, doi:10.1006/jcph.1997.5681.
- 646 Gutfraind, R., and S. B. Savage (1998), Flow of fractured ice through wedge-shaped chan-
 647 nels: smoothed particle hydrodynamics and discrete-element simulations, *Mech. Mat.*,
 648 *29*(1), 1–17, doi:10.1016/s0167-6636(97)00072-0.
- 649 Henann, D. L., and K. Kamrin (2013), A predictive, size-dependent continuum
 650 model for dense granular flows, *Proc. Nat. Acad. Sci.*, *110*(17), 6730–6735, doi:
 651 10.1073/pnas.1219153110.
- 652 Herman, A. (2010), Sea-ice floe-size distribution in the context of spontaneous scaling
 653 emergence in stochastic systems, *Phys. Rev. E*, *81*(6), doi:10.1103/physreve.81.066123.
- 654 Herman, A. (2013), Shear-jamming in two-dimensional granular materials with power-law
 655 grain-size distribution, *Entropy*, *15*(11), 4802–4821, doi:10.3390/e15114802.
- 656 Herman, A. (2016), Discrete-element bonded-particle sea ice model DESIgn, version 1.3a
 657 – model description and implementation, *Geosci. Mod. Dev.*, *9*(3), 1219–1241, doi:
 658 10.5194/gmd-9-1219-2016.
- 659 Hibler, W. D. (1979), A dynamic thermodynamic sea ice model, *J. Phys. Oceanogr.*, *9*(4),
 660 815–846, doi:10.1175/1520-0485(1979)009<0815:adtsim>2.0.co;2.
- 661 Hibler, W. D. (1980), Modeling a variable thickness sea ice cover, *Mon. Weather Rev.*,
 662 *108*(12), 1943–1973, doi:10.1175/1520-0493(1980)108<1943:mavtsi>2.0.co;2.
- 663 Hopkins, M. A. (1996), On the mesoscale interaction of lead ice and floes, *J. Geophys.
 664 Res.: Oceans*, *101*(C8), 18,315–18,326, doi:10.1029/96jc01689.
- 665 Hopkins, M. A. (2004), A discrete element Lagrangian sea ice model, *Eng. Comput.*,
 666 *21*(2/3/4), 409–421, doi:10.1108/02644400410519857.
- 667 Hopkins, M. A., and A. S. Thorndike (2006), Floe formation in arctic sea ice, *J. Geophys.
 668 Res.*, *111*(C11), doi:10.1029/2005jc003352.
- 669 Hopkins, M. A., W. D. Hibler, and G. M. Flato (1991), On the numerical simulation of
 670 the sea ice ridging process, *J. Geophys. Res.*, *96*(C3), 4809, doi:10.1029/90jc02375.
- 671 Horvat, C., and E. Tziperman (2015), A prognostic model of the sea-ice floe size and
 672 thickness distribution, *Cryosphere*, *9*, 2119–2134, doi:10.5194/tc-9-2119-2015.

- 673 Hunke, E. C., and J. K. Dukowicz (1997), An elastic–viscous–plastic model for
674 sea ice dynamics, *J. Phys. Oceanogr.*, *27*(9), 1849–1867, doi:10.1175/1520-
675 0485(1997)027<1849:aevpmf>2.0.co;2.
- 676 Jop, P., Y. Forterre, and O. Pouliquen (2006), A constitutive law for dense granular flows,
677 *Nature*, *441*(7094), 727–730, doi:10.1038/nature04801.
- 678 Kamrin, K., and G. Koval (2014), Effect of particle surface friction on nonlocal consti-
679 tutive behavior of flowing granular media, *Comput. Part. Mech.*, *1*(2), 169–176, doi:
680 10.1007/s40571-014-0018-3.
- 681 Kruggel-Emden, H., M. Sturm, S. Wirtz, and V. Scherer (2008), Selection of an appro-
682 priate time integration scheme for the discrete element method (dem), *Comput. Chem.*
683 *Eng.*, *32*(10), 2263–2279.
- 684 Kwok, R., L. T. Pedersen, P. Gudmandsen, and S. S. Pang (2010), Large sea ice
685 outflow into the Nares Strait in 2007, *Geophys. Res. Lett.*, *37*(3), n/a–n/a, doi:
686 10.1029/2009gl041872.
- 687 Li, B., H. Li, Y. Liu, A. Wang, and S. Ji (2014), A modified discrete element model for
688 sea ice dynamics, *Acta Oceanol. Sin.*, *33*(1), 56–63, doi:10.1007/s13131-014-0428-3.
- 689 Lindsay, R. W., and H. L. Stern (2004), A new lagrangian model of Arc-
690 tic sea ice, *J. Phys. Oceanography*, *34*(1), 272–283, doi:10.1175/1520-
691 0485(2004)034<0272:anlmoa>2.0.co;2.
- 692 Lipscomb, W. H., E. C. Hunke, W. Maslowski, and J. Jakacki (2007), Ridging, strength,
693 and stability in high-resolution sea ice models, *J. Geophys. Res.*, *112*(C3), doi:
694 10.1029/2005jc003355.
- 695 Luding, S. (2008), Introduction to discrete element methods: basic of contact force models
696 and how to perform the micro-macro transition to continuum theory, *Eur. J. Env. Civ.*
697 *Eng.*, *12*(7-8), 785–826.
- 698 Mair, K., K. M. Frye, and C. Marone (2002), Influence of grain characteristics on the fric-
699 tion of granular shear zones, *J. Geophys. Res. Solid Earth*, *107*(B10), ECV–4.
- 700 Martin, T., and A. Adcroft (2010), Parameterizing the fresh-water flux from land ice to
701 ocean with interactive icebergs in a coupled climate model, *Ocean Mod.*, *34*(3-4), 111–
702 124, doi:10.1016/j.ocemod.2010.05.001.
- 703 Menge, J. A. R., and K. F. Jones (1993), The tensile strength of first-year sea ice, *J.*
704 *Glaciol.*, *39*(133), 609–618, doi:10.1017/s0022143000016506.
- 705 Mitchell, J. K., and K. Soga (2005), *Fundamentals of Soil Behavior*, Wiley New York.

- 706 Monaghan, J. J. (2012), Smoothed particle hydrodynamics and its diverse applications,
 707 *Annual Rev. Fluid Mech.*, *44*(1), 323–346, doi:10.1146/annurev-fluid-120710-101220.
- 708 Morgan, J. K. (1999), Numerical simulations of granular shear zones using the distinct
 709 element method 2. Effects of particle size distribution and interparticle friction on me-
 710chanical behavior, *J. Geophys. Res.*, *104*(B2), 2721–2732.
- 711 Morgan, J. K. (2015), Effects of cohesion on the structural and mechanical evolution of
 712 fold and thrust belts and contractional wedges: Discrete element simulations, *J. Geo-
 713phys. Res.: Solid Earth*, *120*(5), 3870–3896, doi:10.1002/2014jb011455.
- 714 Nakayama, Y., and R. F. Boucher (1998), *Introduction to Fluid Mechanics*, Elsevier, doi:
 715 10.1016/b978-034067649-3/50003-8.
- 716 Nedderman, R. M. (1992), *Statics and Kinematics of Granular Materials*, Cambridge Uni-
 717versity Press, Cambridge.
- 718 Obermayr, M., K. Dressler, C. Vrettos, and P. Eberhard (2013), A bonded-particle model
 719 for cemented sand, *Comput. Geotech.*, *49*, 299–313, doi:10.1016/j.compgeo.2012.09.001.
- 720 Peters, I. R., J. M. Amundson, R. Cassotto, M. Fahnestock, K. N. Darnell, M. Truffer, and
 721 W. W. Zhang (2015), Dynamic jamming of iceberg-choked fjords, *Geophys. Res. Lett.*,
 722 *42*(4), 1122–1129, doi:10.1002/2014gl062715.
- 723 Petrovic, J. J. (2003), Review: Mechanical properties of ice and snow, *J. Mat. Sci.*, *38*(1),
 724 1–6.
- 725 Potyondy, D. O., and P. A. Cundall (2004), A bonded-particle model for rock, *Int. J. Rock
 726Mech. Min.*, *41*(8), 1329–1364.
- 727 Radjaï, F., and F. Dubois (2011), *Discrete-Element Modeling of Granular Materials*, 425
 728 pp., Wiley-Iste.
- 729 Rallabandi, B., Z. Zheng, M. Winton, and H. A. Stone (2017a), Wind-driven formation of
 730 ice bridges in straits, *Phys. Rev. Lett.*, *118*(12), doi:10.1103/physrevlett.118.128701.
- 731 Rallabandi, B., Z. Zheng, M. Winton, and H. A. Stone (2017b), Formation of sea ice
 732 bridges in narrow straits in response to wind and water stresses, *J. Geophys. Res.:
 733Oceans*, *122*(7), 5588–5610, doi:10.1002/2017jc012822.
- 734 Rampal, P., S. Bouillon, E. Ólason, and M. Morlighem (2016), neXtSIM: a new La-
 735 grangian sea ice model, *Cryosphere*, *10*(3), 1055–1073, doi:10.5194/tc-10-1055-2016.
- 736 Reynolds, O. (1885), On the dilatancy of media composed of rigid particles in contact,
 737 *Philos. Mag.*, *20*(5), 46.

- 738 Robel, A. A. (2017), Thinning sea ice weakens buttressing force of iceberg mélange and
739 promotes calving, *Nature Commun.*, 8, 14,596, doi:10.1038/ncomms14596.
- 740 Rothrock, D. A. (1975), The energetics of the plastic deformation of pack ice by ridging,
741 *J. Geophys. Res.*, 80(33), 4514–4519, doi:10.1029/jc080i033p04514.
- 742 Rudnicki, J. W., and J. R. Rice (1975), Conditions for the localization of deformation in
743 pressure-sensitive dilatant materials, *J. Mech. Phys. Solids*, 23(6), 371–394.
- 744 Samelson, R. M., T. Agnew, H. Melling, and A. Münchow (2006), Evidence for atmo-
745 spheric control of sea-ice motion through Nares Strait, *Geophys. Res. Lett.*, 33(2), doi:
746 10.1029/2005gl025016.
- 747 Schulson, E., A. Fortt, D. Iliescu, and C. Renshaw (2006), On the role of frictional sliding
748 in the compressive fracture of ice and granite: Terminal vs. post-terminal failure, *Acta*
749 *Mat.*, 54(15), 3923–3932, doi:10.1016/j.actamat.2006.04.024.
- 750 Schulson, E. M. (1999), The structure and mechanical behavior of ice, *JOM*, 51(2), 21–27,
751 doi:10.1007/s11837-999-0206-4.
- 752 Schulson, E. M. (2001), Brittle failure of ice, *Eng. Fract. Mech.*, 68(17-18), 1839–1887,
753 doi:10.1016/s0013-7944(01)00037-6.
- 754 Schulson, E. M., and A. L. Fortt (2012), Friction of ice on ice, *J. Geophys. Res.*,
755 117(B12), doi:10.1029/2012jb009219.
- 756 Steer, A., A. Worby, and P. Heil (2008), Observed changes in sea-ice floe size distribu-
757 tion during early summer in the western weddell sea, *Deep Sea Res. Part II: Top. Stud.*
758 *Oceanogr.*, 55(8-9), 933–942, doi:10.1016/j.dsr2.2007.12.016.
- 759 Tang, J., S. Sagdiphour, and R. P. Behringer (2009), Jamming and flow in 2d hoppers, in
760 *AIP Conf. Proc.*, AIP, doi:10.1063/1.3179975.
- 761 Terzaghi, K., R. B. Peck, and G. Mesri (1996), *Soil Mechanics in Engineering Practice*,
762 John Wiley & Sons.
- 763 Thomas, C. C., and D. J. Durian (2015), Fraction of clogging configurations sampled by
764 granular hopper flow, *Phys. Rev. Lett.*, 114(17), doi:10.1103/physrevlett.114.178001.
- 765 Thorndike, A. S., D. A. Rothrock, G. A. Maykut, and R. Colony (1975), The
766 thickness distribution of sea ice, *J. Geophys. Res.*, 80(33), 4501–4513, doi:
767 10.1029/jc080i033p04501.
- 768 To, K., P.-Y. Lai, and H. K. Pak (2001), Jamming of granular flow in a two-dimensional
769 hopper, *Phys. Rev. Lett.*, 86(1), 71–74, doi:10.1103/physrevlett.86.71.

- 770 Tremblay, L.-B., and L. A. Mysak (1997), Modeling sea ice as a granular material, in-
771 cluding the dilatancy effect, *J. Phys. Oceanogr.*, *27*(11), 2342–2360, doi:10.1175/1520-
772 0485(1997)027<2342:msiaag>2.0.co;2.
- 773 Weiss, J., and E. M. Schulson (2009), Coulombic faulting from the grain scale to the
774 geophysical scale: lessons from ice, *J. Phys. D: Appl. Phys.*, *42*(21), 214,017, doi:
775 10.1088/0022-3727/42/21/214017.
- 776 Weiss, J., E. M. Schulson, and H. L. Stern (2007), Sea ice rheology from in-situ, satellite
777 and laboratory observations: Fracture and friction, *Earth Planet. Sci. Lett.*, *255*(1-2), 1–
778 8, doi:10.1016/j.epsl.2006.11.033.
- 779 Wilchinsky, A. V., and D. L. Feltham (2006), Modelling the rheology of sea ice as a
780 collection of diamond-shaped floes, *J. Non-Newton. Fluid Mech.*, *138*(1), 22–32, doi:
781 10.1016/j.jnnfm.2006.05.001.
- 782 Wilchinsky, A. V., D. L. Feltham, and M. A. Hopkins (2010), Effect of shear rup-
783 ture on aggregate scale formation in sea ice, *J. Geophys. Res.*, *115*(C10), doi:
784 10.1029/2009jc006043.
- 785 Wilchinsky, A. V., D. L. Feltham, and M. A. Hopkins (2011), Modelling the reorienta-
786 tion of sea-ice faults as the wind changes direction, *Ann. Glaciol.*, *52*(57), 83–90, doi:
787 10.3189/172756411795931831.
- 788 Zuriguel, I. (2014), Invited review: Clogging of granular materials in bottlenecks, *Pap.*
789 *Phys.*, *6*(0), doi:10.4279/pip.060014.